PAPER • OPEN ACCESS

Observation of electron-scale turbulence suppression under weak magnetic shear with neon seeding in EAST plasma

To cite this article: Y.Q. Chu *et al* 2023 *Nucl. Fusion* **63** 086021

OPEN ACCESS
IOP Publishing | International Atomic Energy Agency
Nuclear Fusion
Nucl. Fusion **63** (2023) 086021 (9pp)
https://doi.org/10.1088/1741-4326/acdd83

Observation of electron-scale turbulence suppression under weak magnetic shear with neon seeding in EAST plasma

Y.Q. Chu[1], B.S. Zhang[2], P. Li[2,*], X.D. Yang[2,*], H.Q. Liu[2], Y.X. Jie[2], C.B. Wu[2], W.M. Zhang[2,3], K.D. Li[2], T.F. Zhou[2], L. He[2,3], Q. Zang[2], H. Lian[2], F.B. Zhong[1,2], R.J. Zhu[2,3], L. F. Zhang[3], K. Hanada[4] and the EAST Team[a]

[1] College of Physics and Optoelectronic Engineering, Shenzhen University, Shenzhen 518060, China
[2] Institute of Plasma Physics, Chinese Academy of Sciences, Hefei 230031, China
[3] University of Science and Technology of China, Hefei 230026, China
[4] Research Institute for Applied Mechanics, Kyushu University, Kasuga 816-8580, Japan

E-mail: lipan@ipp.ac.cn and xdyang@ipp.ac.cn

Received 22 March 2023, revised 25 May 2023
Accepted for publication 12 June 2023
Published 3 July 2023

Abstract

Improved confinement caused by Ne injection is investigated in EAST. The safety factor q profile and electron-scale turbulence are studied with a polarimeter-interferometer system and CO_2 laser collective scattering system in a series of Ne injection experiments in EAST. Ne with a suitable injection rate can lead to negative magnetic shear in the plasma core, which promotes electron-scale turbulence suppression. The continuous injection of Ne under the reversed shear condition further reduces the electron-scale turbulence intensity. Core electron temperature increase and confinement improvement are observed. QuaLiKiz is applied to model the influence of an impurity and reversed q on turbulence. The combination of stabilization effects of negative magnetic shear and Ne on turbulence is much stronger than the impurity's own effect, which could explain the experimentally observed electron temperature (T_e) increase and turbulence suppression. Besides, the relationship between pedestal structure induced by Ne injection and lower hybrid wave (LHW)-driven current deposition is discussed. These results provide a new perspective to improve the confinement in the case of Ne injection, i.e. to adjust the Ne injection to modify the ideal plasma equilibrium.

Keywords: electron-scale turbulence, magnetic shear, neon seeding, confinement, tokamak

(Some figures may appear in colour only in the online journal)

[a] See Wan *et al* 2017 (https://doi.org/10.1088/1741-4326/aa7861) for the EAST Team.
[*] Authors to whom any correspondence should be addressed.

1. Introduction

The divertor heat load in ITER will exceed by several times the tolerable plasma-facing material limits [1]. One of the envisaged solutions is to use impurity seeding (such as nitrogen (N), argon (Ar) and neon (Ne)) to form a steady-state edge radiation layer, and this has been proved in ASDEX Upgrade [2–4], JET [5, 6], DIII-D [7], JT-60 U [8, 9] and Alcator C-Mod [10, 11]. The impurity ions can greatly enhance the radiation losses and plasma dilution resulting in lower fusion power [12–17]. However, the impurity effect has been observed in tokamaks with a degree of confinement improvement in the plasma core [15, 18–23]. However, the role of impurities in transport is hitherto unrecognized.

The main theoretical progress has so far been devoted to the anomalous transport of energy, primarily induced by drift wave instabilities such as ion temperature gradient (ITG) modes [24] and electron temperature gradient modes [25], trapped electron modes (TEMs) [26], and kinetic ballooning mode. The analysis of impurity impacts on turbulence is of particular interest as impurity induced turbulence suppression is a potential candidate responsible for the impurity included confinement improvement. Turbulence measurements have been compared with theory calculations for DIII-D and indicate that the impurity content can influence the linear stability of the long-wavelength modes [27]; one plausible explanation of this experimental finding is Ne injection leads to $\boldsymbol{E} \times \boldsymbol{B}$ velocity shear suppression [28]. The numerical results indicate that impurity effects on the turbulence depend on the density profile, temperature profile and the dynamics of the impurity ions [29]. Impurity ions have substantially destabilizing (stabilizing) effects on TEMs in isotope plasmas for $L_{\rm ez} \equiv L_{\rm ne}/L_{\rm nz} > 0$ (<0), opposite to the case of ITG-driven modes [30]. Impurity mode and the ITG could be strongly coupled to each other [31]. Theoretical work shows that impurity ions could significantly decrease the frequency of the geodesic acoustic mode (GAM) and increase its damping [32], resulting in enhanced turbulent transport [33–35].

Electron-scale turbulence (such as TEM turbulence) tends to be an important contributor to anomalous transport in present and future fusion experiments that rely on powerful electron heating. Theoretically, negative (reversed) or low magnetic shear act to reduce high-k turbulence growth rates, thus facilitating electron-scale turbulence reduction [36–38]. Impurity injection could modestly change the profiles of density, temperature and current. Impurity induced magnetic shear effects on turbulence have also attracted some attention recently. The formation of a negative shear q profile in DIII-D creates the conditions for internal transport barrier (ITB) generation by lowering the pressure profile of the pedestal to allow more current to be deposited in the core [18]. The numerical result indicates the impurity could lead to a more stable TEM instability under negative magnetic shear [30]. The effects of the impurity ions on electron-scale turbulence and the underlying mechanisms have not been experimentally identified so far, in particular considering the effect of magnetic shear.

This paper will systematically present the characteristics of electron-scale turbulence after Ne seeding on EAST, and the results support Ne seeding rate playing an important role in the evolution of the current profile that influences the electron-scale turbulence. The rest of this paper is organized as follows: section 2 introduces the experimental setup and the relationship between Ne injection and confinement improvement is the focus of section 3, followed by the simulation results in section 4. The reason for the equilibrium variation is discussed in section 5. Finally, a brief conclusion is given in section 6.

2. Experimental setup

Experiments were performed on EAST, which has a major radius of 1.85 m and a minor radius 0.45 m [39]. The maximum plasma current of EAST is 1 MA and the maximum toroidal magnetic field is 3.5 T. EAST can be operated with upper single null (USN), lower single null and double null configurations. Abundant plasma heating systems are available on EAST, including an lower hybrid wave (LHW) system with 2.45 GHz and 4.6 GHz [40], an electron cyclotron resonance heating (ECRH) system which has strong spatial localization of power deposition [41], an ion cyclotron resonance heating system [42] and a neutral beam injection (NBI) system with four beam lines in which two are co-direction and two are contrary direction [43]. These heating methods can also drive the current. The discharges used in this paper were selected from the same campaign of experiments in 2018. All discharges are of USN configuration with a toroidal field of about 2.5 T. LHW, NBI and ECRH are the main auxiliary heating methods.

A Thomson scattering (TS) system is used to provide $T_{\rm e}$ profiles [44], while $T_{\rm e}$ evolution is observed with anelectron cyclotron emission (ECE) system [45]. The toroidal field is suitable for the ECE system and the ECE data matches well with TS. Ion temperature was measured by an x-ray imaging crystal spectrometer (XCS) system [46]. An extreme ultraviolet spectrometer (EUV) system was applied to directly measure Ne content in the core of the plasma [47]. The change in Ne content plays an important role in these experiments. The polarimeter-interferometer (POINT) system has 11 horizontal measurement chords, with each spaced 8.5 cm apart, symmetrically covering most of the plasma [48]. The POINT system can measure line-integrated electron density and Faraday rotation angle simultaneously and, by using this information as an additional constraint in EFIT code, the safety factor q and the current profile can be inferred [49]. Turbulence is monitored by a CO_2 laser collective scattering system [50]. Electron-scale turbulences with $k_\theta = 12$ cm^{-1} and $k_\theta = 22$ cm^{-1} in the plasma core $\rho = 0-0.4$ are monitored by the diagnostics in the experiments.

Improved confinement is observed after Ne injection in a typical shot #80443. Figure 1 shows the basic parameters of this shot. Plasma current $I_{\rm p}$ is 450 kA and toroidal field is 2.5 T. The impurity is injected as a gas mixture from the upper outer divertor target and the gas is a 5% Ne and 95% D_2 in this shot. The triggering time for impurity injection is 4 s and the time delay is about 100 ms. At 4.3 s, the feedback control system starts to intervene and the Ne level increases slowly. For the sake of illustration, we define the fast injection phase

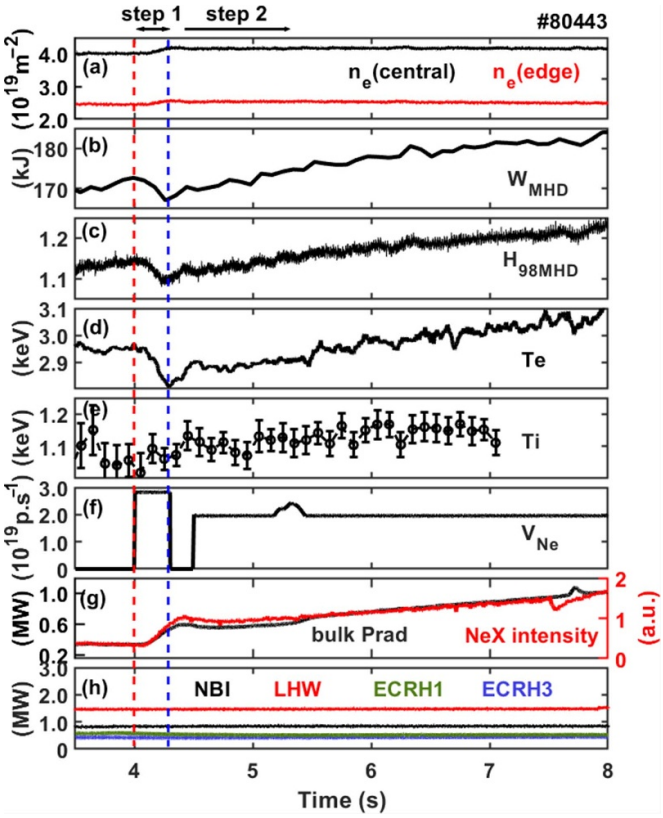

Figure 1. Parameters of shot #80443. (*a*) Line integrated electron density (n_e) measured by POINT system. Black line is the result of chord 6 and red line is the result of chord 1, which are core and boundary density, respectively. (*b*) plasma stored energy W_{MHD}, (*c*) confinement quality H_{98}, (*d*) evolution of core electron temperature measured by ECE system, (*e*) evolution of core ion temperature (T_i) measured by XCS system, (*f*) Ne seeding rate (V_{Ne}) from the upper outer divertor, (*g*) total radiation power (Prad) and intensity of NeX measured by EUV system, (*h*) heating power of RF waves and NBI. The region between vertical red dotted line and vertical blue dotted line is defined as step 1, which is rapid injected phase of Ne. The time period after the blue vertical dashed line is defined as step 2, which is the feedback control phase, where Ne content rises more slowly.

of Ne between 4 s and 4.3 s as step 1, which is enclosed by the red and the blue verrtical dotted lines in figure 1, and we define the feedback control phase after 4.3 s as step 2, which includes the right-hand side of the blue dotted line in figure 1. The Ne seeding rate from the upper out divertor is shown in figure 1(*f*), while it should be noted that the seeding rate is not linear with the Ne content change rate in the core. Figure 1(*a*) shows the line integrated density measured by the POINT system: the black line is the result of chord 6 with measured the position at $Z = 0$ cm, and the blue line is the result of chord 1 with measured the position at $Z = 42.5$ cm. After Ne is injected, both core and boundary density rise transiently (as shown in figure 1(*a*)). Plasma density is stable in step 2. Ne is fully ionized under these discharge conditions, and therefore NeX intensity was used to label the amount of Ne in the plasma. The relative intensity of NeX is shown in figure 1(*g*). The total radiation power shows the same trend as the Ne content (shown in figure 1(*g*)). Injected Ne causes a certain amount of radiation loss. Plasma storage energy and the plasma confinement factor drop transiently after 4 s (figures 1(*b*) and (*c*)).

At step 2, although total plasma radiation intensity continuing to increase, the plasma stored energy and H_{98} are increasing and exceed the levels before Ne injection. Specifically, the plasma stored energy increases from 170 kJ to 185 kJ, while heating power keeps constant as shown in figure 1(*h*). In step 2, T_e in plasma core continuously increases (figure 1(*d*)), while T_i and n_e do not show notable variation. The increase of T_e may be the main factor of storage energy increase.

3. Relationship between Ne injection and confinement improvement

Statistics results of Ne injection experiments with similar discharge conditions are studied. In these shots, we define two steps as in #80443. In step 1, plasma pressure and current has been redistributed. At the end of step 1, a new equilibrium has been established. The plasma evolution in step 2 is based on the equilibrium of step 1.

3.1. Relationship between Ne injection and T_e increase

Figure 2 shows the evolution of relative Ne content variation in data base. Blue, green and red lines correspond to slow, suitable and fast speed of the increase in Ne content, respectively. Figure 3 shows the relation of Ne content change rate and T_e change rate. Ne content change rate is defined as NeX intensity change rate normalized by electron density and plasma current. And change rate of electron temperature is calculated in step 2.

In figure 3, red dashed line identifies the location where electron temperature change is zero. The two vertical black dashed lines enclose an interval of rising rate of Ne content, in which electron temperature increases, while outside the interval, electron temperature tends to decrease. In the experimental conditions, there is a suitable range of Ne content change rate. Within this range, the injection of Ne can lead to electron temperature increase. Shots within the interval are corresponding to the green lines in figure 2, shots with Ne content change rate below and exceed the interval are corresponding to the blue and red lines in figure 2, respectively. Different Ne content change rates in the step 1 (0.3 s) can result in different plasmas states in step 2 (shown in figure 3).

3.2. Relationship between Ne injection and turbulence

Electron-scale turbulence dominate anomalous transport in electron-heating dominated EAST experiments [51–53]. Turbulences at electron-scale ($1 < k_\theta \rho_s < 2$) in plasma core ($\rho \sim 0 - 0.4$) are monitored by the CO_2 laser collective scattering system. To research the nature of plasma after Ne seeding, turbulence evolution is studied in two phases.

Figure 4 shows the evolution of turbulence with Ne injection in step 1. In this step, T_e decreases and amplitude of electron-scale turbulence (at $k_\theta = 12$ cm^{-1}) behaves differently. There is an interval in which turbulence is suppressed

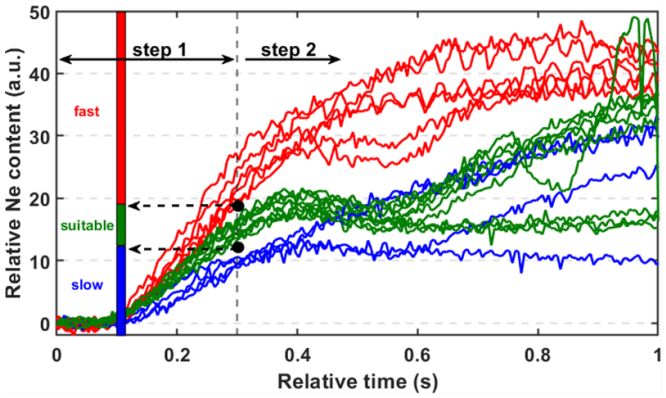

Figure 2. Relative Ne content evolution in the data base. X axis is relative time, $t = 0$ s is defined as Ne injection time. Three different colored curves represent different Ne content change rate, where red lines are fast Ne seeding rates, green lines are suitable Ne seeding rates, and blue lines are slow Ne seeding rates. The different color curves correspond to the corresponding color points in figure 3. With different Ne seeding rates, the electron temperature has different trends.

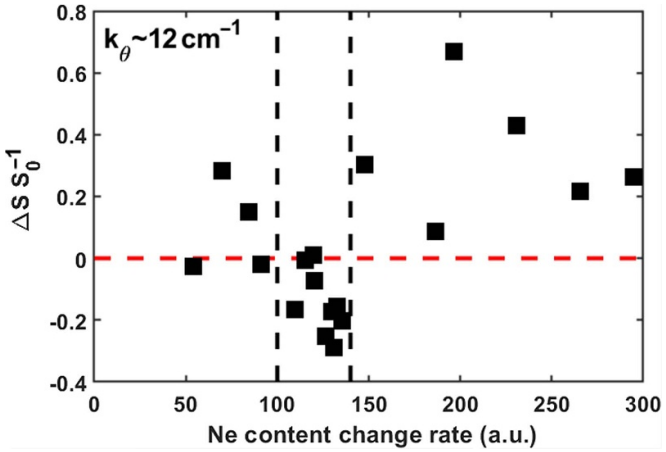

Figure 3. Relation of Ne content change rate to relative variation of turbulence amplitude with $k_\theta = 12$ cm^{-1} at step 1. Here, $\Delta S = S_1 - S_0$, where S_1 and S_0 are the amplitude of turbulence measured by CO_2 system at the end and beginning of step 1.

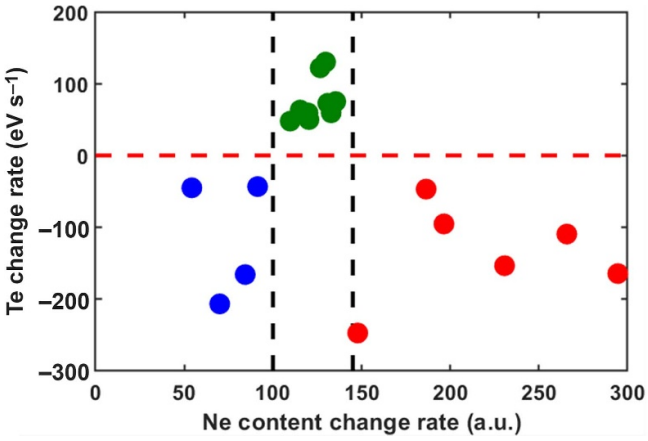

Figure 4. Relation of Ne content change rate to electron temperature change rate. (The color of the marker matches with figure 2).

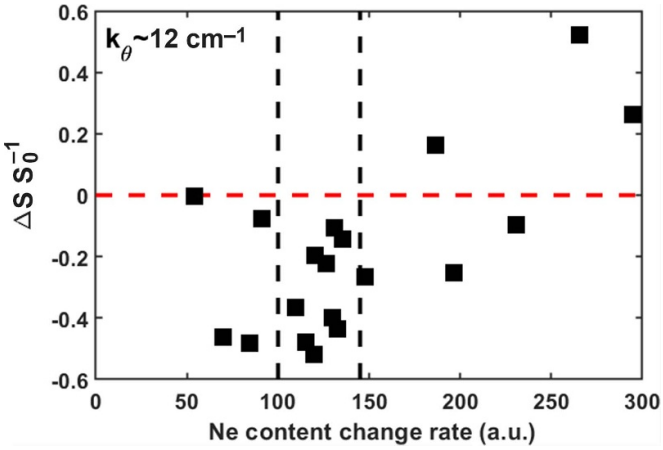

Figure 5. Relation of Ne content change rate to relative variation of turbulence amplitude with $k_\theta = 12$ cm^{-1} at step 2. Here, $\Delta S = S_1 - S_0$, where S_1 and S_0 are the amplitude of turbulence measured by CO_2 system at the end and beginning of step 2.

with high probability. Turbulence suppression implies confinement improvement. It is worth noting that the interval is the same as that shown in figure 3. Figure 5 shows the evolution of turbulence with Ne injection in step 2. In step 2, all electron-scale turbulence in the interval is further suppressed, the maximum reduction of integrated turbulence power is half. And the average reduction ratio is about 30%, which is higher than that outside the interval. Turbulence suppression in step 1 and step 2 may be the reason of T_e increase in step 2.

There may be some mechanisms that promote turbulence suppression in the first stage and are favorable for turbulence suppression in the second stage. These mechanisms are associated with Ne seeding at a certain rate. Turbulence is driven by free energy in plasma, Ne seeding may redistribute the free energy in the plasma or introduce some kind of turbulence suppression mechanism (such as $\boldsymbol{E} \times \boldsymbol{B}$ flows, magnetic shear, etc). The possible mechanism behind the turbulence evolution in this interval is described in the next section.

3.3. *Magnetic field shears evolution after Ne injection*

There are several factors that could affect the turbulence, including Shafranov shift, impurity itself and magnetic shear and so on. Magnetic shear in this interval is studied in this section. Magnetic shear evolution could be monitored by POINT system. Figures 6(*a*) and (*b*) show the line integrated density and Faraday rotation angle before (3.9 s) and after (4.3 s) step 1 in #80443. Data of chords at $Z = 35$ cm and $Z = -17$ cm do not shown here as laser loss are too much in this shot of these two chords. For POINT measurement, Faraday rotation angle is expressed as $\Psi_F = 2.62 \times 10^{-13} \lambda^2 \int n_e B_{||} dl$. Ψ_F is Faraday rotation angle in each chord, λ is laser wavelength, for POINT system the λ is 432 μm, n_e is plasma density and $B_{||}$ is the poloidal magnetic field parallel to the diagnostic chords. Comparing the data of 3.9 s and 4.3 s, line integrated density shows slight increase in all chords. In general, increase of density will bring the increase of absolute value of Faraday rotation angle when the magnetic field shows

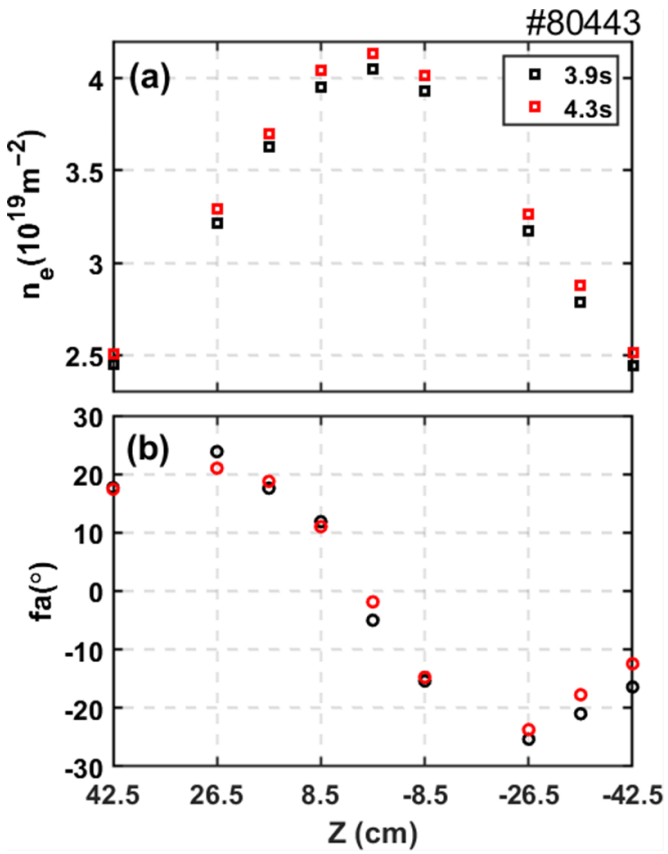

Figure 6. Comparison of (*a*) line integrated density, (*b*) Faraday rotation angle before (black, 3.9 s) and after (red, 4.3 s) Ne injection.

not much changes. Error of measurement by stray light has been eliminated offline. Therefore, absolute value of Faraday rotation angle in chords at $Z = 8.5$ cm and $Z = 0$ cm shown in figure 6(*b*) should be from the variation of poloidal field. Because five and six channels cross the central position of plasma, they have the longest length through the plasma, and optical paths of the two channels and plasma boundary connecting the two channels can form a loop when viewed from the perspective of a poloidal profile. On the one hand, plasma boundary is sufficiently short with respect to the optical path, and on the other hand the polar magnetic field at the boundary is relatively weak, so the loop can be conceived as an Ampere loop, whereby the magnitude of toroidal current between five or six channels, the strength of toroidal current in the core, is reflected. Ampere's law $\oint_L B_\theta \cdot \mathrm{d}l = \mu_0 I_\phi$ is applied here, where L is length of the loop, B_θ is poloidal field and I_ϕ is toroidal current. By this method it can be easily observed that this decrease in core ring current is prevalent in the discharges where the temperature of the electrons is counted to rise. Core current reduction implies an increase in q_0.

The q profile of 3.9 s and 4.3 s are shown in figure 7. The calculation is based on EFIT code and using POINT measurement as additional constraint. The q profile of 3.9 s shows a positive shear while after Ne injection, due to the reduction of core current, q_0 increases and q profile evolved into a weak reversed shear. The $q_{\min}$ position is near ρ about 0.2 where the electron temperature rises fastest. Reversed magnetic shear could be the reason of electron-scale turbulence suppression, meanwhile simulation in the next section shows the effect of reversed magnetic shear on turbulence suppression.

4. Simulation

To the underlying mechanism for experimental observations, latest updated QuaLiKiz [54, 55] is applied to model the influence of impurity and observed reversed q on turbulences. In QuaLiKiz, TEM and ITG are included with poloidal wave number spectrum $k_x\rho_s$ in the range of 0.1–2, with $\rho_s = m_s v_{\mathrm{th},s}/(eB)$, and radial wave number is taken at $k_x\rho_s = 0$. Quasilinear weight is given by $\gamma/ < k_\perp^2 >$, with the operator $< >$ being an average over mode structure along field line. Electron, deuterium (main ions) and carbon are included in the modeling. lack of impurities' density profile measurement, carbon's content is calculated from Z_{eff}. Ne is also included for the phase with impurity seeding and its content is calculated from the additional increased Z_{eff} (δZ_{eff}). Density profiles of Ne is set to be same as n_{e}. No toroidal rotation is included.

As shown in figure 7, reversed q begins to appear at $\rho \sim 0.2$, where T_{e} also increases most evidently. Thus, the simulation is focused on this position and the basic parameters are listed in table 1. The data are chosen from shot #80443 at 3.9 s with positive q profile and Ne is not seeding in this moment.

As shown in figure 8, TEM can be found from $k_x\rho_s \sim 0.3-1.2$. Influences of Ne and weakly reversed .q induced by Ne seeding in step 1 are compared by including Ne with $\delta Z_{\mathrm{eff}} = 0.2$ and replacing the q profile with the weakly reversed q ($q = 1.58$, $\hat{s} = -0.02$), separately. It can be seen in figure 8 that turbulence can be both stabilized by Ne and reversed q, but stabilization effect of latter is more evident, implying in the first step the reversed q is the main contributor to stabilize TEM. This agrees well with experimental observation that turbulence is observed to be stabilized in the case with reversed q.

To study the Ne effect on turbulence evolution in step 2, $\delta Z_{\mathrm{eff}} = 0.8$ are included with positive and negative magnetic shear, respectively. As shown in figure 9, it is found that when Ne is included in the case with reversed q profile turbulence can be further stabilized, which is consistent with experimental observations as shown in figure 5. On the other hand, combined with reversed q profile, Ne could further suppress the turbulence than it act alone, especially in the range of low $k_x\rho_s$ which drives more significant electron heat flux. This could explain the experimental observation of T_{e} and turbulence variation tendency. In the case without reversed q profile, it is also expected to observe higher T_{e} due to the turbulence suppression from Ne itself. While the negative result should be from the reason that the stabilization effect cannot compensate energy loss brought by the cooling effect from Ne radiation. Ne impurity could lead to a more stable TEM instability under negative magnetic shear. And finite cooling effect by Ne radiation combined with efficiently TEM suppression with the reversed q in the interval, leading to higher T_{e}.

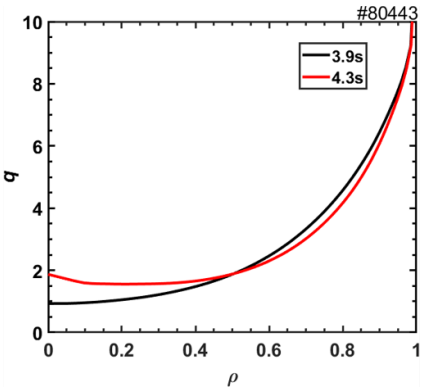

Figure 7. Calculated q profiles before (black, 3.9 s) and after (red, 4.3 s) Ne injection.

Table 1. Parameters for # 80443 at 3.9 s. Here, $L_{T_e} = -\left(\frac{1}{T_e}\frac{\partial T_e}{\partial R}\right)^{-1}$, $L_{T_i} = -\left(\frac{1}{T_i}\frac{\partial T_i}{\partial R}\right)^{-1}$, $L_{n_e} = -\left(\frac{1}{n_e}\frac{\partial n_e}{\partial R}\right)^{-1}$, $\hat{s}$ is the magnetic shear and ν^* is collisional rate.

ρ	T_e/T_i	R/L_{ne}	R/L_{Te}	R/L_{Ti}	$\hat{s}$	q	Z_{eff}	ν^*
0.2	2.17	4	12	2	0.19	1.02	1.65	0.4

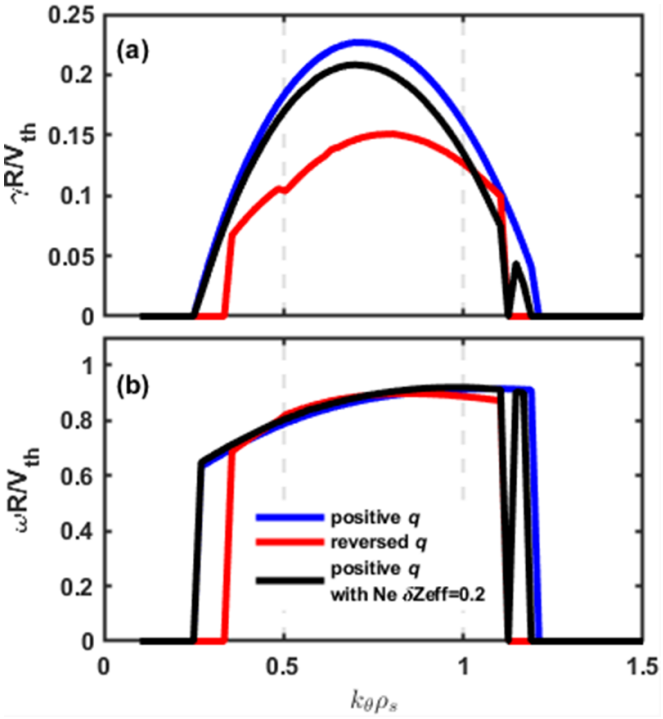

Figure 8. Simulation of step 1. Comparison of normalized (a) growth rate and (b) frequency of TEM in different conditions. Blue line is the simulation result from basic parameters with positive q profile shown in table 1. Red line and black lines are the simulation results of changing the magnetic shear and $\delta Z_{\rm eff} = 0.2$.

5. Discussion

Control of magnetic shear is an important topic for the operation of future devices and fusion reactors. Modulation of the current profile can change the safety factor distribution. In this paper we have shown that the presence of weak reversed magnetic shear contributes to the increase in core electron temperature. A suitable rate of increase for Ne content could influence the current distribution. For #80443 we propose a conjecture. As on-axis ECRH and NBI always drive the current in the core, current distribution variation in the core could be from the change of LHW deposition and bootstrap current distribution. The bootstrap current is related to the pressure profile. When Ne is injected, electron density in the core shows little increase, while T_e and T_i decline. Variation of core pressure could lead to a change of the core bootstrap current distribution. On the other hand, the efficiency of LHW could be affected by effective charge number $Z_{\rm eff}$, pedestal density and the average plasma temperature. All these factors could be changed after Ne injection. Comparison of the deposition current of LHW before and after Ne injection has been made using GERAY and CQL3D code [56]. Results are shown in figure 10. Before Ne injection, there is a part of the LHW driving current in the core region, while after Ne injection this part of the current decreases, leading to a reduction of the total deposited current in the core. In order to verify which parameter plays a greater role in the condition of shot #80443, different parameters are changed artificially and other parameters kept constant, and LHW deposition distributions are studied.

In figure 10, with higher $Z_{\rm eff}$ (blue line), the LHW deposition distribution is nearly the same as that at 3.9 s. The

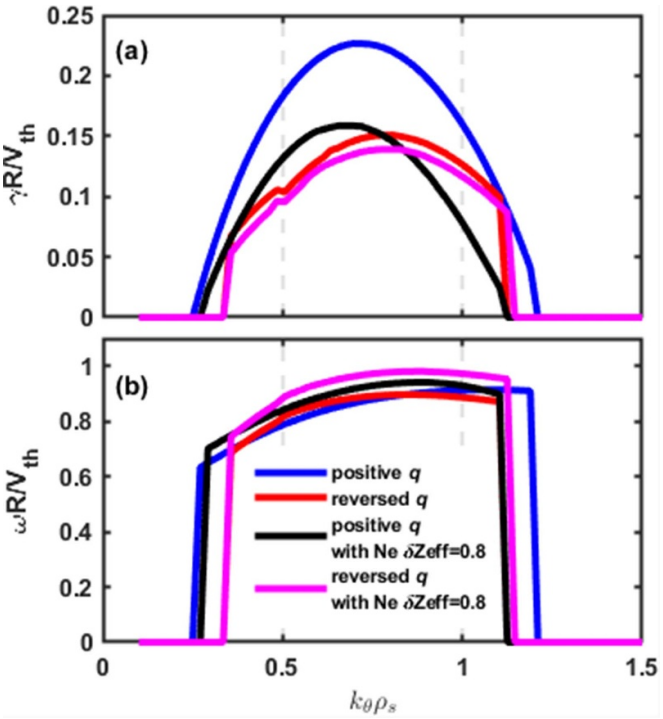

Figure 9. Simulation of step 2. Comparison of normalized (a) growth rate and (b) frequency of TEM in different conditions. Blue line is the simulation result from basic parameters with positive q profile shown in table 1. Red line is the simulation result with reversed magnetic shear. Black and pink lines are the simulation results of changing $\delta Z_{\rm eff} = 0.8$ in positive and negative magnetic shear conditions, respectively.

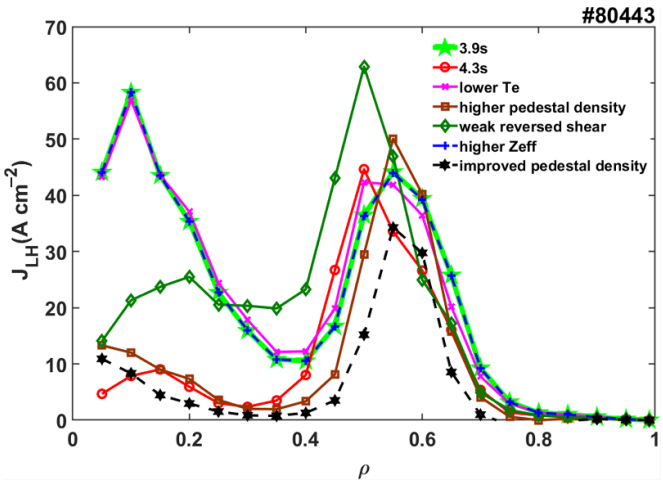

Figure 10. Deposition of LHW before (3.9 s, light green line with pentagram mark) and after (4.3 s, red line with circle mark) Ne injection. Based on the profiles of 3.9 s, the deposition distribution of LHW is calculated by changing different parameters separately. The pink line is the result by using T_e at 4.3 s which is lower than 3.9 s. The brown line with square marks is the result of using the n_e profile at 4.3 s, which has higher pedestal density than at 3.9 s. The dark green line with diamond marks is the result of using the q profile at 4.3 s which has weak reversed magnetic shear. The blue line with cross marks is the result of using Z_{eff} at 4.3 s. The black dotted line with hexagram marks is the result of using the n_e profile which has much higher pedestal density than 4.3 s.

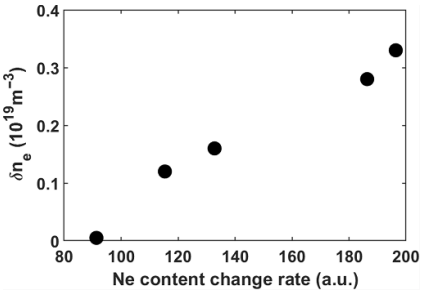

Figure 11. Electron density change in the pedestal of five typical shots.

result with lower T_e (pink line) shows little difference from the result at 3.9 s. This implies that these two factors are not the key factors in this condition. The q profile at 3.9 s is replaced by the q profile at 4.3 s, and the result, shown in a dark green color in figure 10, indicates that reversed magnetic shear could reduce LHW-driven current in the core region, while the LHW-driven current deposits much more in the outer. The brown line is the result of using a density profile of 4.3 s, with higher pedestal density than 3.9 s; LHW-driven current deposition shows a clear reduction in the core. Further increase of pedestal density is shown by black dotted line in figure 10, as LHW-driven current deposition reduces in the whole region. LHW-driven current deposition is sensitive to the pedestal density and higher pedestal density will stop the wave from penetrating deeper, thus deposition of LHW in the core shows a reduction in figure 10. Figure 11 shows the relation of pedestal density and Ne content change rate in typical shots: with higher Ne content change rate, the pedestal density could be even higher. Pedestal density is an important factor that affects the deposition of LHW-driven current. This may be the reason for the appearance of reversed magnetic shear with a finite rate of increase for the Ne content.

The control of LHW deposition position is an important problem. Based on the idea that the pedestal density regulates the position of LHW current deposition, Li injection [57], plasma configuration [58] and supersonic molecular beam injection [59] may also be the means of LHW generating off-axis current. More experiments could be done in the future to verify it.

6. Conclusion

In summary, a study of Ne injection with improved confinement has been performed on EAST. Ne injection with a finite rate can change the equilibrium with reversed magnetic shear of the plasma and promote improvement of the confinement. A reversed q profiles can lead to a reduction of turbulence, which has been proved by the CO_2 laser collective scattering system. These experimental results are supported by simulation using QuaLiKiz code. Simulation results show that Ne impurity can lead to a more stable TEM instability under negative magnetic shear. A finite cooling effect by Ne radiation, combined with efficient TEM suppression with the reversed q in the interval, may be the reason for higher T_e and confinement improvement. Impurity injection induced pedestal structure change leads to the varition of LHW-driven current deposition is also discussed.

A new perspective on impurity injection-induced confinement improvement is presented. For the ITER-like RF heating tokamak, equilibrium reestablishment by impurity injection should be considered. Maximizing the beneficial effect of impurity injection and allowing it to be dominant in front of the deleterious effects of impurity injection could help us to promote better plasma confinement. To promote rather a positive impact of impurities on fusion power, it is necessary to further study the influence of impurity injection on the pedestal and the influence of impurity injection on turbulence suppression. Exploring suitable impurity injection methods is important for future fusion devices.

Acknowledgments

This research was supported by the National Key R&D Program of China (Grant Nos. 2019YFE03040003 and 2022YFE03050003), by the National Nature Science Foundation of China (Grant Nos. 12175277, 12105319, 11975271), and by the HFIPS Director's Fund, Grand No. YZJJKX202301. Funding for this work was also provided in part by the Collaborative Research Program of the Research Institute for Applied Mechanics, Kyushu University, by the Major Special Science and Technology Project of Anhui Province (Grant No. 912188707023).

ORCID iDs

Y.Q. Chu https://orcid.org/0000-0002-7379-0117
X.D. Yang https://orcid.org/0000-0003-1681-6330
H.Q. Liu https://orcid.org/0000-0001-6892-358X
K.D. Li https://orcid.org/0000-0003-0486-7368
L. He https://orcid.org/0000-0001-5980-9654

References

[1] Pitts R.A. *et al* 2019 Physics basis for the first ITER tungsten divertor *Nucl. Mater. Energy* **20** 100696
[2] Reimold F., Wischmeier M., Bernert M., Potzel S., Kallenbach A., Müller H.W., Sieglin B. and Stroth U. 2015 Divertor studies in nitrogen induced completely detached H-modes in full tungsten ASDEX Upgrade *Nucl. Fusion* **55** 033004
[3] Kallenbach A. *et al* 2010 Divertor power load feedback with nitrogen seeding in ASDEX Upgrade *Plasma Phys. Control. Fusion* **52** 055002
[4] Schweinzer J. *et al* 2011 Confinement of 'improved H-modes' in the all-tungsten ASDEX Upgrade with nitrogen seeding *Nucl. Fusion* **51** 113003
[5] Giroud C. *et al* 2013 Impact of nitrogen seeding on confinement and power load control of a high-triangularity JET ELMy H-mode plasma with a metal wall *Nucl. Fusion* **53** 113025
[6] Maddison G.P. *et al* 2014 Contrasting H-mode behaviour with deuterium fuelling and nitrogen seeding in the all-carbon and metallic versions of JET *Nucl. Fusion* **54** 073016
[7] Petrie T.W. *et al* 2008 Comparison of radiating divertor behaviour in single-null and double-null plasmas in DIII-D *Nucl. Fusion* **48** 045010
[8] Ishijima T., Kubo H., Shimada M., Konoshima S., Higashijima S., Hosogane N., Sakasai A., Itami K. and Sugie T. 1999 Radiation and spectroscopy analysis of divertor discharges with neon gas puff in JT-60U *Plasma Phys. Control. Fusion* **41** 1155
[9] Higashijima S., Asakura N., Kubo H., Miura Y., Nakano T., Konoshima S., Itami K., Sakurai S., Takenaga H. and Tamai H. 2003 Control of divertor heat load by Ar injection with keeping high performance in ELMy H-mode plasmas on JT-60U *J. Nucl. Mater.* **313–316** 1123–30
[10] Loarte A. *et al* 2011 High confinement/high radiated power H-mode experiments in Alcator C-Mod and consequences for international thermonuclear experimental reactor (ITER) QDT = 10 operation *Phys. Plasmas* **18** 056105
[11] Reinke M.L., Hughes J.W., Loarte A., Brunner D., Hutchinson I.H., LaBombard B., Payne J. and Terry J.L. 2011 Effect of N2, Ne and Ar seeding on Alcator C-Mod H-mode confinement *J. Nucl. Mater.* **415** S340–4
[12] Leonard A.W., Makowski M.A., McLean A.G., Osborne T.H. and Snyder P.B. 2015 Compatibility of detached divertor operation with robust edge pedestal performance *J. Nucl. Mater.* **463** 519–23
[13] Kallenbach A. *et al* 2015 Partial detachment of high power discharges in ASDEX Upgrade *Nucl. Fusion* **55** 053026
[14] Ishida S. *et al* 1997 Achievement of high fusion performance in JT-60U reversed shear discharges *Phys. Rev. Lett.* **79** 3917–21
[15] Gruber O. *et al* 1995 Observation of continuous divertor detachment in H-mode discharges in ASDEX Upgrade *Phys. Rev. Lett.* **74** 4217–20
[16] Asakura N., Nakano T., Oyama N., Sakamoto T., Matsunaga G. and Itami K. 2009 Investigations of impurity seeding and radiation control for long-pulse and high-density H-mode plasmas in JT-60U *Nucl. Fusion* **49** 115010
[17] Bernert M. *et al* 2017 Power exhaust by SOL and pedestal radiation at ASDEX Upgrade and JET *Nucl. Mater. Energy* **12** 111–8
[18] Wang L. *et al* 2021 Integration of full divertor detachment with improved core confinement for tokamak fusion plasmas *Nat. Commun.* **12** 1365
[19] Lazarus E.A. *et al* 1984 Confinement improvement in beam heated ISX-B discharges with low-z impurity injection *J. Nucl. Mater.* **121** 61–68
[20] Messiaen A.M. *et al* 1996 High confinement and high density with stationary plasma energy and strong edge radiation in the TEXTOR-94 tokamak *Phys. Rev. Lett.* **77** 2487–90
[21] Hill K.W. *et al* 1999 Tests of local transport theory and reduced wall impurity influx with highly radiative plasmas in the tokamak fusion test reactor *Phys. Plasmas* **6** 877–84
[22] McKee G., Burrell K., Fonck R., Jackson G., Murakami M., Staebler G., Thomas D. and West P. 2000 Impurity-induced suppression of core turbulence and transport in the DIII-D tokamak *Phys. Rev. Lett.* **84** 1922–5
[23] Jackson G.L. *et al* 1999 Enhanced confinement discharges in DIII-D with neon and argon induced radiation *J. Nucl. Mater.* **266–269** 380–5
[24] Lin Z., Hahm T.S., Lee W.W., Tang W.M. and White R.B. 1998 Turbulent transport reduction by zonal flows: massively parallel simulations *Science* **281** 1835–7
[25] Dorland W., Jenko F., Kotschenreuther M. and Rogers B.N. 2000 Electron temperature gradient turbulence *Phys. Rev. Lett.* **85** 5579–82
[26] Roach C.M., Connor J.W. and Janjua S. 1995 Trapped particle precession in advanced tokamaks *Plasma Phys. Control. Fusion* **37** 679
[27] McKee G.R. *et al* 2000 Impurity-induced turbulence suppression and reduced transport in the DIII-D tokamak *Phys. Plasmas* **7** 1870–7
[28] Murakami M. *et al* 2001 Physics of confinement improvement of plasmas with impurity injection in DIII-D *Nucl. Fusion* **41** 317
[29] Du H., Wang Z.-X. and Dong J.Q. 2015 Impurity effects on short wavelength ion temperature gradient mode in elongated tokamak plasmas *Phys. Plasmas* **22** 022506
[30] Du H., Wang Z.-X. and Dong J.Q. 2016 Impurity effects on trapped electron mode in tokamak plasmas *Phys. Plasmas* **23** 072106
[31] Dong J.Q. and Horton W. 1995 Studies of impurity mode and ion temperature gradient mode in toroidal plasmas *Phys. Plasmas* **2** 3412–9
[32] Xie B., Guo W. and Xiang N. 2018 Impurity effect on geodesic acoustic mode in toroidally rotating tokamak plasmas *Plasma Phys. Control. Fusion* **60** 025015
[33] Kong D.F. *et al* 2013 Evolutions of zonal flows and turbulence in a tokamak edge plasma during electron cyclotron resonance heating *Nucl. Fusion* **53** 123006
[34] Storelli A. *et al* 2015 Comprehensive comparisons of geodesic acoustic mode characteristics and dynamics between Tore Supra experiments and gyrokinetic simulations *Phys. Plasmas* **22** 062508
[35] Zenin V.N. *et al* 2016 Plasma potential and geodesic acoustic mode evolution with helium puffing in the ECRH regime on the T-10 tokamak *J. Phys. Conf. Ser.* **747** 012005
[36] Levinton F.M. *et al* 1995 Improved confinement with reversed magnetic shear in TFTR *Phys. Rev. Lett.* **75** 4417–20
[37] Hugon M. *et al* 1992 Shear reversal and MHD activity during pellet enhanced performance pulses in JET *Nucl. Fusion* **32** 33
[38] Strait E.J. *et al* 1995 Enhanced confinement and stability in DIII-D discharges with reversed magnetic shear *Phys. Rev. Lett.* **75** 4421–4

[39] Li J. *et al* 2013 A long-pulse high-confinement plasma regime in the Experimental Advanced Superconducting Tokamak *Nat. Phys.* **9** 817–21
[40] Liu F.K. *et al* 2016 Development of 4.6 GHz lower hybrid current drive system for steady state and high performance plasma in EAST *Fusion Eng. Des.* **113** 131–8
[41] Xu H. *et al* 2019 Recent progress of the development of a long pulse 140GHz ECRH system on EAST *EPJ Web Conf.* **203** 04002
[42] Zhang X.J. *et al* 2022 First experimental results with new ICRF antenna in EAST *Nucl. Fusion* **62** 086038
[43] Hu C. *et al* 2015 Overview of development status for EAST-NBI system *Plasma Sci. Technol.* **17** 817
[44] Zang Q., Zhao J., Yang L., Hu Q., Xi X., Dai X., Yang J., Han X., Li M. and Hsieh C.L. 2011 Upgraded multipulse laser and multipoint Thomson scattering diagnostics on EAST *Rev. Sci. Instrum.* **82** 063502
[45] Han X., Liu X., Liu Y., Domier C.W., Luhmann N.C., Li E.Z., Hu L.Q. and Gao X. 2014 Design and characterization of a 32-channel heterodyne radiometer for electron cyclotron emission measurements on Experimental Advanced Superconducting Tokamak *Rev. Sci. Instrum.* **85** 073506
[46] Shi Y. *et al* 2010 Imaging x-ray crystal spectrometer on EAST *Plasma Phys. Control. Fusion* **52** 085014
[47] Xu Z. *et al* 2021 An extreme ultraviolet spectrometer working at 10–130 Å for tungsten spectra observation with high spectral resolution and fast-time response in Experimental Advanced Superconducting Tokamak *Nucl. Instrum. Methods Phys. Res.* A **1010** 165545
[48] Liu H.Q. *et al* 2016 Initial measurements of plasma current and electron density profiles using a polarimeter/interferometer (POINT) for long pulse operation in EAST (invited) *Rev. Sci. Instrum.* **87** 11D903
[49] Qian J. *et al* 2017 EAST equilibrium current profile reconstruction using polarimeter-interferometer internal measurement constraints *Nucl. Fusion* **57** 036008
[50] Li P. *et al* 2020 Study of turbulence modulation and core density peaking with CO_2 laser collective scattering diagnostics in the EAST tokamak *Nucl. Fusion* **60** 066001
[51] Wu M.Q. *et al* 2018 Transport simulation of EAST long-pulse H-mode discharge with integrated modeling *Nucl. Fusion* **58** 046001
[52] Wu M.Q. *et al* 2019 Modeling and advances in the high bootstrap fraction regime on EAST towards the steady-state operation *Nucl. Fusion* **59** 106009
[53] Gong X.Z. *et al* 2022 EAST steady-state long pulse H-mode with core-edge integration for CFETR *Nucl. Fusion* **62** 076009
[54] Bourdelle C., Citrin J., Baiocchi B., Casati A., Cottier P., Garbet X. and Imbeaux F. 2016 Core turbulent transport in tokamak plasmas: bridging theory and experiment with QuaLiKiz *Plasma Phys. Control. Fusion* **58** 014036
[55] Stephens C.D. 2021 Advances in quasilinear gyrokinetic modeling of turbulent transport *PhD Thesis* University of California, Los Angeles
[56] Smirnov A.P. and Harvey R.W. 1995 Calculations of the current drive in DIII-D with the GENRAY ray tracing code *Bull. Am. Phys. Soc.* **40** 1837
[57] Osborne T.H. *et al* 2015 Enhanced H-mode pedestals with lithium injection in DIII-D *Nucl. Fusion* **55** 063018
[58] Dunne M.G. *et al* 2017 The role of the density profile in the ASDEX-Upgrade pedestal structure *Plasma Phys. Control. Fusion* **59** 014017
[59] Yang Z.C. *et al* 2016 Effect of supersonic molecular beam injection deposition on edge localized mode mitigation in the HL-2A H-mode plasmas *Phys. Plasmas* **23** 012515